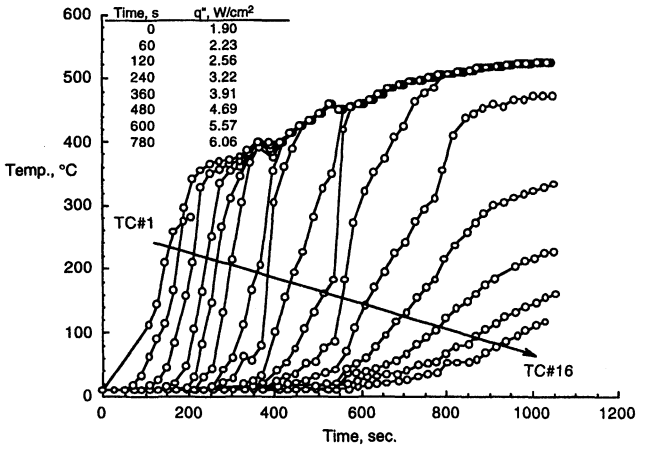

Fig. 5 Temperature distributions for heat pipe startup from the frozen state (test 3) (T = ±0.75%).

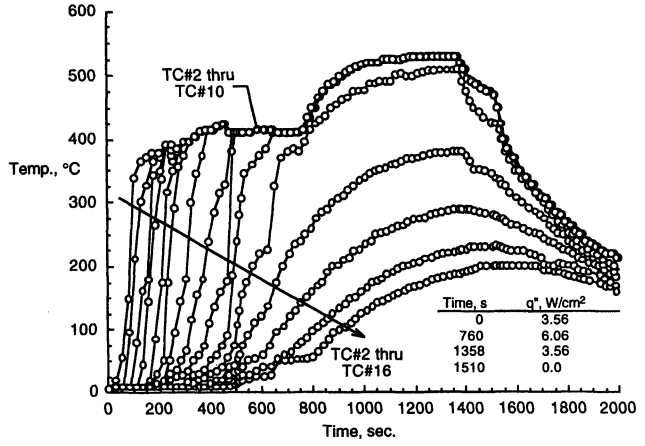

Fig. 6 Temperature distributions for heat pipe startup from the frozen state (test 4) (T = ±0.75%).

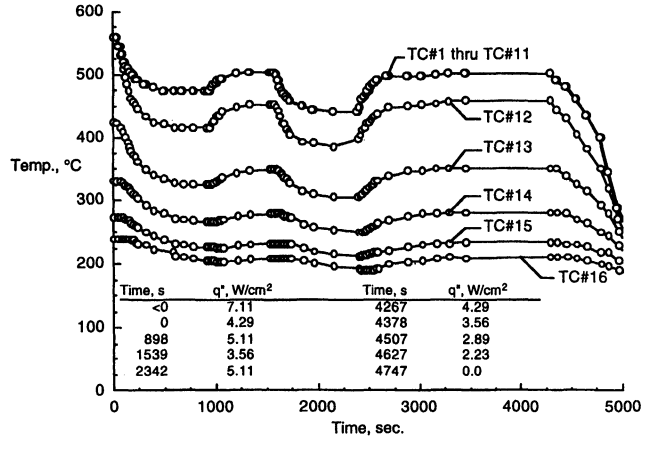

Fig. 7 Temperature distributions for the heat pipe during transient testing (T = ±0.75%).

increased from 6.06 to 6.57 W/cm^2. Shortly after the increase, a hot spot appeared in the evaporator region. Prior to the hot spot, TC No. 1–11 were all isothermal.

In test 4, the heat flux initially was stepped up to 3.56 W/cm^2, then increased to 6.06 W/cm^2, and then was decreased back to 3.56 W/cm^2 before being turned off. Thermocouple No. 1 is not included with the transient data, shown in Fig. 6, because it was not operating properly. Prior to increasing the heat flux to 6.06 W/cm^2, the heat pipe was isothermal through TC No. 11. Even after the heat flux was increased to 6.06 W/cm^2, TC No. 12 did not reach the isothermal temperature of the rest of the heat pipe.

One test is presented where the heat pipe was operating at steady-state initially and the heat flux was then increased and decreased several times, as shown in Fig. 7. The heat pipe was initially operating at a steady-state temperature of 565°C with an applied heat flux of 7.11 W/cm^2 in the evaporator region. Thermocouple No. 12 was nearly the same temperature as the isothermal portion of the heat pipe for $t < 0$ s. Once the heat flux was decreased at $t = 0$ s, the temperature at TC No. 12 rapidly decreased below that of the isothermal portion of the heat pipe. Because the heat flux was not increased back to the 7.11 W/cm^2 value, TC No. 12 did not reach the heat-pipe operating temperature during this test. Thermocouple Nos. 1–11 remained isothermal throughout the test.

Concluding Remarks

A Nb–1%Zr heat pipe with potassium working fluid was tested under steady-state, transient, and relatively rapid startup conditions. The heat pipe was heated by rf induction heating up to a temperature of 675°C and a throughput of 600 W. The heat pipe and the tests were well-characterized so that the data may be used for comparison with analysis. Temperatures and heat fluxes were recorded on a time scale of seconds to reduce the computer time required for code validation.

Acknowledgment

The authors would like to thank the Thermal Structures Branch of NASA Langley Research Center for funding this work under contract NAS1-19317.

References

[1]Woloshun, K. A., Sena, J. T., Keddy, E. S., and Merrigan, M. A., "Radial Heat Flux Limits on Potassium Heat Pipes: An Experimental and Analytical Investigation," 7th Symposium on Space Nuclear Power Systems, Albuquerque, NM, Jan. 1990; also Los Alamos National Laboratory Rept. LA-UR-89-3365, 1989.

[2]Woloshun, K. A., Sena, J. T., Keddy, E. S., and Merrigan, M. A., "Boiling Limits in Heat Pipes with Annular Gap Wick Structures," AIAA Paper 90-1793, June 1990.

View Factor for Ring Elements on Coaxial Cylinders

C. P. Tso* and S. P. Mahulikar†
Nanyang Technological University, Nanyang Avenue, Singapore 639798, Singapore

Nomenclature

A = surface area, m^2
d = distance, m
F_{i-j} = view factor of surface j as seen by surface i
L = length, m
r = radius, m

Subscripts

ab = annular disk of inner radius r_i and outer radius r_s at bottom surface
au = annular disk of inner radius r_i and outer radius r_s at upper surface

Received March 9, 1998; revision received May 20, 1998; accepted for publication June 24, 1998. Copyright © 1998 by the American Institute of Aeronautics and Astronautics, Inc. All rights reserved.

*Associate Professor, School of Mechanical and Production Engineering. E-mail: mcptso@ntu.edu.sg.

†Graduate Student, School of Mechanical and Production Engineering.

si = shell interior surface
sid = shell interior surface of length *d*
te = tube exterior surface
ted = tube exterior surface of length *d*
a = annular disk surface of inner radius r_t and outer radius r_s
b = bottom surface
e = exterior surface
i = interior surface/intermediate between shell and tube (between r_t and r_s)
s = shell surface
t = tube surface
u = upper surface
1 = element 1
2 = element 2

Superscripts
(1) = view factors derived by approach 1
(2) = view factors derived by approach 2

Introduction

THE analytical evaluation of the view factor gets complicated with geometry and its numerical evaluation is cumbersome in practical applications involving systems discretized into a large number of spatial meshes. Although software packages like FACET and VIEW[1] compute the view factors numerically for complicated configurations, it is always advantageous to have closed-form analytical solutions wherever possible to reduce the computation time and tedium, and to obtain insights of geometrical parameter dependence.

Coaxial cylinders are common to several practical applications and for analyzing the radiant heat exchange among their surfaces, they are discretized into coaxial ring elements. Reid and Tennant[2] evaluated a single numerical integration after three analytical integrations of the defining quadruple line integral, for ring surface elements on coaxial cylinders. Rea[3] analytically derived the view factor between the outside of an end-capped cylinder to an annular disk plugged at its bottom. Howell[4] provided the view factors for an exhaustive coverage of geometries, some in the form of analytical expressions and some as numerical approximations or graphical solutions. The view factor algebra outlined by Rea for the exterior surface of a cylinder of smaller radius to the interior surface of a coaxial cylinder of larger radius (configuration I in Fig. 1) was used to obtain an analytical solution. Their compilation includes some numerical results of Reid and Tennant for ring elements of equal lengths on coaxial cylinders (configuration II in Fig. 1). Shukla and Ghosh[5] derived the view factors between various surfaces of an enclosure bounded partly by two coaxial cylinders of different lengths and comprising an end capped tube; the configuration considered by Rea is among them.

Srinivasan and White[6] derived the differential view factor between differential rings on the tube exterior and the shell interior surfaces of coaxial cylinders. These differential view factors were numerically integrated to obtain the view factors between finite length ring surfaces, and compared with the numerical results of Reid and Tennant. Although they have not addressed the issue raised here, their statements could be construed to infer that the view factors for configurations I and II in Fig. 1 are different. Furthermore, if the view factors for configurations I and II were known to be identical, then the effort in deriving an analytical expression for the view factor between differential rings on the shell interior and tube exterior surfaces and then numerically integrating to obtain the view factors for finite length rings would be known to them as redundant.[2,6] This difference is also reflected in the separate compilation of Howell (configurations C-93 and C-95, for I and II, respectively), in which an analytical solution is provided for configuration C-93 and the numerical results of Reid and Tennant for configuration C-95. There are no two identical configurations compiled separately by Howell for which an analytical solution is provided for one and a numerical solution for the other. Hence, it is concluded that though an analytical solution is reported for configuration I (configuration C-93[4]), it has always been thought to be different from configuration II. This Note proves the equality of the view factors for configurations I and II, conceptually and by view factor algebra.

Equality of View Factors for Configurations I and II

Figure 2 shows two elements (1 and 2) of discretized coaxial cylinders, giving two surfaces on the tube exterior *te*1 and *te*2, and two surfaces on the shell interior *si*1 and *si*2. Because of

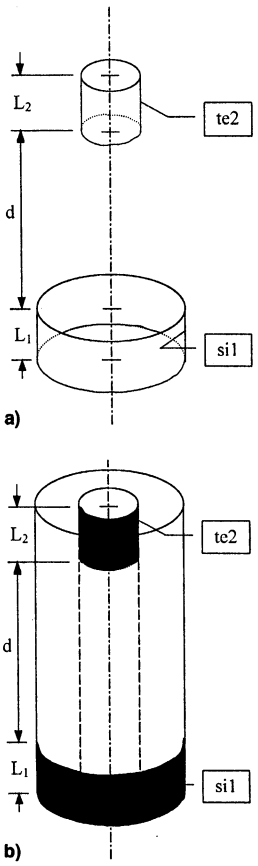

Fig. 1 Configurations of coaxial cylinders: a) configuration I and b) configuration II.

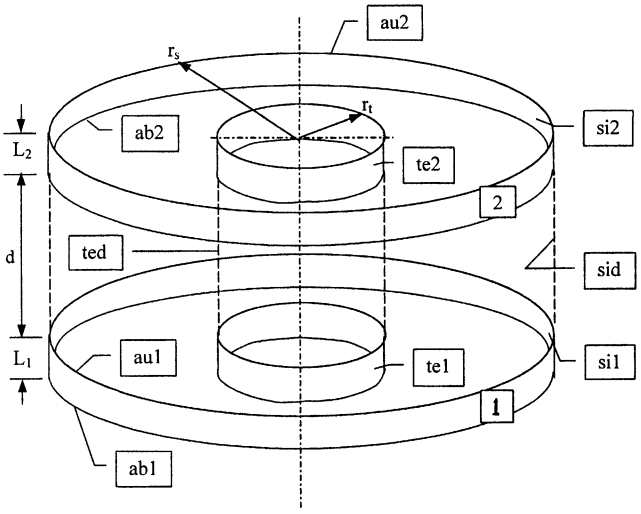

Fig. 2 Surfaces of coaxial cylinder elements.

spacing d between the two elements, additional surfaces *sid* and *ted* are also shown. In addition, four annular disk surfaces (*au*1, *ab*1, *au*2, and *ab*2) of inner radius r_t and outer radius r_s, which are enclosing the elements, are also shown.

The view factor is based on geometric optics in which it is assumed that radiation propagates in a straight line, and it contains only the direct contribution of the radiation, i.e., the contribution of the reflected radiation is not considered. It is mathematically defined as an integral over the two surfaces exchanging radiation. The ray bundles emitted from surface *te*2, which can directly reach surface *si*1 and can determine the area ranges among which radiation can be exchanged, are exactly the same for configurations I and II and they are not influenced by the obstruction in configuration II. The integrand in the view factor is the product of the direction cosines related to two points on the surfaces connected by a ray bundle divided by the square of the distance between these two points. Hence, the integration ranges and the integrands are the same for configurations I and II. Nevertheless, because the view factors for configurations I and II have been assumed to be different,[4,6] as stated in the Introduction, the following proof establishing their equality is presented.

The essential difference between configurations I and II is the presence of the obstructing tube in configuration II. It will be proved that this difference does not matter for the view factor $F_{te1-si2}$. The view factor is split by two different approaches. In the first approach, the view factor is split into view factors of two surfaces without obstruction, and in the second approach, the view factor is split into view factors affected by the presence of the obstructing tube. Because the literature assumes these two approaches to give different results, they are denoted by superscripts (1) and (2), respectively.

Approach 1 (Independent of Obstruction)

By the conservation of radiant energy emitted by surface te1 towards surface si2,

$$F^{(1)}_{te1-si2} = F^{(1)}_{te1-ab2} - F^{(1)}_{te1-au2} = (A_a/A_{te1}) \cdot [F^{(1)}_{ab2-te1} - F^{(1)}_{au2-te1}] \quad (1)$$

Equation (1) implies that if the imaginary surface *ab*2 is removed, the radiation incident on it from surface *te*1 will either be incident on the imaginary surface *au*2 or on the surface *si*2. By the conservation of radiant energy emitted by surfaces *ab*2 and *au*2 toward surface *te*1

$$F^{(1)}_{ab2-te1} = F_{ab2-(te1+ted)} - F_{ab2-ted} \quad (2a)$$

$$F^{(1)}_{au2-te1} = F_{au2-(te1+ted+te2)} - F_{au2-(ted+te2)} \quad (2b)$$

The superscript is not indicated for the view factors on the right-hand side (RHS) of Eqs. (2a) and (2b), because these view factors are between the exterior of a cylinder to an annular disk plugged at its bottom, and have been analytically derived and plotted by Rea.[3] There is no obstruction between the surfaces and, hence, no ambiguity. From Eqs. (2a) and (2b), it is evident that the view factors $F^{(1)}_{ab2-te1}$ and $F^{(1)}_{au2-te1}$ are unaffected by the inner cylinder of length L_1 being capped or not, as the view factors between the imaginary annular disk surfaces of element 2 and the cap radius r_t are not featured. From Eqs. (1), (2a), and (2b)

$$F^{(1)}_{te1-si2} = (A_a/A_{te1}) \cdot \{[F_{ab2-(te1+ted)} - F_{ab2-ted}] - [F_{au2-(te1+ted+te2)} - F_{au2-(ted+te2)}]\} \quad (3)$$

Approach 2 (with Obstruction)

Similar to Eq. (1)

$$F^{(2)}_{te1-si2} = (A_a/A_{te1}) \cdot [F^{(2)}_{ab2-te1} - F^{(2)}_{au2-te1}] \quad (4a)$$

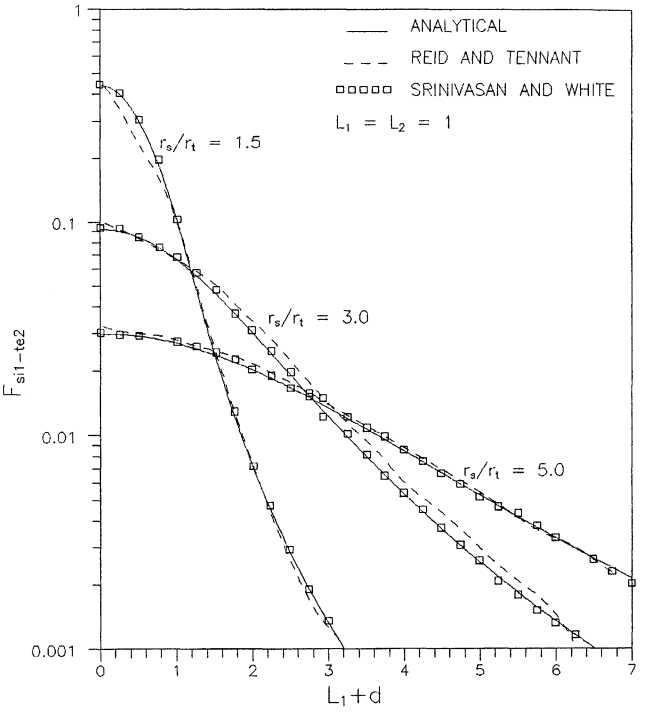

Fig. 3 View factors for configurations I and II, comparison with numerical results.

where the obstructing tube is now assumed to affect the view factors in Eq. (4a). By the conservation of radiant energy emitted by surfaces *ab*2 and *au*2 toward surface *te*1

$$F^{(2)}_{ab2-te1} = F_{ab2-au1} - F_{ab2-ab1} - F_{ab2-si1} \quad (4b)$$

$$F^{(2)}_{au2-te1} = F_{au2-au1} - F_{au2-ab1} - F_{au2-si1} \quad (4c)$$

The superscript is not indicated on the view factors on the RHS of Eqs. (4b) and (4c) because it is known unambiguously that the obstructing tube affects these view factors and their values would be higher in the absence of the tube. From Eqs. (4a–4c)

$$F^{(2)}_{te1-si2} = (A_a/A_{te1}) \cdot [(F_{ab2-au1} - F_{ab2-ab1} - F_{ab2-si1}) - (F_{au2-au1} - F_{au2-ab1} - F_{au2-si1})] \quad (5a)$$

If the view factor $F_{te1-si2}$ is not affected by the presence of the obstructing tube, $F^{(1)}_{te1-si2}$ given by Eq. (3) must be the same as $F^{(2)}_{te1-si2}$ given by Eq. (5a). By the enclosure rule

$$F_{ab2-au1} = 1 - F_{ab2-ted} - F_{ab2-sid} \quad (5b)$$

$$F_{ab2-ab1} = 1 - F_{ab2-(te1+ted)} - F_{ab2-(si1+sid)} \quad (5c)$$

$$F_{au2-au1} = 1 - F_{au2-(ted+te2)} - F_{au2-(sid+si2)} \quad (5d)$$

$$F_{au2-ab1} = 1 - F_{au2-(te1+ted+te2)} - F_{au2-(si1+sid+si2)} \quad (5e)$$

From Eqs. (5b) and (5c), and by the conservation of radiant energy

$$F_{ab2-au1} - F_{ab2-ab1} = F_{ab2-(te1+ted)} - F_{ab2-ted} + F_{ab2-si1} \quad (6)$$

Similarly

$$F_{au2-au1} - F_{au2-ab1} = F_{au2-(te1+ted+te2)} - F_{au2-(ted+te2)} + F_{au2-si1} \quad (7)$$

From Eqs. (5a), (6), and (7), $F^{(2)}_{te1-si2}$ is written as

$$F^{(2)}_{te1-si2} = (A_a/A_{te1}) \cdot \{[F_{ab2-(te1+ted)} - F_{ab2-ted}] - [F_{au2-(te1+ted+te2)} - F_{au2-(ted+te2)}]\} \quad (8)$$

Comparing Eqs. (3) and (8) shows $F^{(1)}_{te1-si2} = F^{(2)}_{te1-si2}$ and, hence, completes the proof that the obstructing tube does not affect the view factor from a tube exterior surface to a shell interior surface. The view factors of configurations I and II are identical. Because an analytical solution for the view factor of configuration I has been provided by Howell,[4] the same can be used for configuration II. Figure 3 shows the comparison of the analytical solution (configuration I) with the numerical results of Reid and Tennant,[2] and the numerical results of Srinivasan and White[6] (both of configuration II). The indication that the analytical solution compares well with the numerical results supports the proof.

Concluding Remarks

The view factors for configurations I and II are proved to be identical. The view factors for configuration II, based on the analytical solution reported for configuration I, agree with the numerical results reported for configuration II. The analytical solution for configuration I can be used to obtain the view factor for configuration II.

Acknowledgment

The authors gratefully acknowledge the support provided by the National Science and Technology Board of Singapore, Project Number JTARC 5/96.

References

[1]Emery, A. F., Johansson, O., Lobo, M., and Abrous, A., "A Comparative Study of Methods for Computing the Diffuse Radiation Viewfactors for Complex Structures," *Journal of Heat Transfer*, Vol. 113, 1991, pp. 413–422.

[2]Reid, R. L., and Tennant, J. S., "Annular Ring View Factors," *AIAA Journal*, Vol. 11, No. 10, 1973, pp. 1446–1448.

[3]Rea, S. N., "Rapid Method for Determining Concentric Cylinder Radiation View Factors," *AIAA Journal*, Vol. 13, No. 8, 1975, pp. 1122, 1123.

[4]Howell, J. R., *A Catalog of Radiation Configuration Factors*, McGraw–Hill, New York, 1982.

[5]Shukla, K. N., and Ghosh, D., "Radiation Configuration Factors for Concentric Cylinder Bodies," *Indian Journal of Technology*, Vol. 23, 1985, pp. 244–246.

[6]Srinivasan, R., and White, A.C., "Analytical Expression for a Concentric-Cylinder Radiation View Factor," *Journal of Thermophysics and Heat Transfer*, Vol. 10, No. 3, 1996, pp. 534–536.

Effects of Contact and Spreading Resistance on Heat Sink Cooling Performance

J. G. Maveety*
Intel Corporation, Santa Clara, California 95052

Introduction

IN a system's environment, the junction temperature of a semiconductor device depends on the thermal resistance between the die, heat-sinking material, and ambient. To ensure the junction temperature will be maintained within a safe operating region, the thermal resistance must be reduced at the same rate that the power is dissipated. Consequently, understanding the contributors to the total thermal resistance helps in the design of thermal management.

In this work, experiments were conducted to investigate the effects of heat sink fin geometry and material selection on the cooling of a silicon test chip. The apparatus was instrumented so that the contributions to the total thermal resistance could be measured. Closed-form analytical expressions were used to predict the average thermal spreading resistance within the heat sink and the die-heat sink contact resistance.

Experiment Setup, Procedure, and Uncertainty Analysis

Two different heat sink pin arrays and materials were studied. Identical carbon composite and aluminum heat sinks were milled to have a square base measuring 50.8 × 50.8 mm. All of the fins were square and measured ($d \times d$). The fin-to-fin spacing, s, varied as the number of fins, n, were changed (see Table 1).

All heat sink contact surfaces were subjected to a grinding process that produced an rms surface roughness of 0.203 μm (8 μin.). The flatness of the heat sinks was 4 mil/in. The heat sinks were instrumented with four 36-gauge copper-constantan thermocouples. As shown in Fig. 1, one thermocouple, T_b, was placed 1.0 mm from the base, and the remaining three thermocouples, T_c, were placed 1.0 mm from the top of the heat sink base plate. The silicon thermal test chip has its own internal thermal diode that was used to measure the junction temperature, T_j. All measurements were collected using a NetDaq data-acquisition system.

The silicon test chip was an OLGA (organic land grid array) type, measuring 12 × 12 mm and capable of generating 30 W. The test chip was placed into an electrical contactor that was attached to an FR-4 load board. The setup is illustrated in Fig. 1. A dc power supply provided power input to the test chip. The contactor and load board were backed by a fiber-insulating board to minimize the heat loss through the bottom and sides of the apparatus. The heat sinks were placed on top of the test chip and loaded to give a constant die to sink contact force of 25 N for all experiments. This ensured good electrical contact between the test chip and contactor as well as good test chip to heat sink thermal contact. It is a well-documented fact that thermal contact resistance decreases with increased contact pressure; however, for OLGA packages, realistic limits of contact pressure are limited to ensure that solder joint attach and package surfaces are not damaged.

Steady-state air-impingement flow experiments were conducted with a round nozzle of diameter D = 6.4 mm. The results presented here were performed with $Re_D = 4.5 \times 10^4$.

Table 1 Fin numbers and spacing of arrays used in experiments[a]

$n \times n$	7 × 7	13 × 13
d	5.08	2.03
s	2.54	2.03

[a]Numerical values are in millimeters.

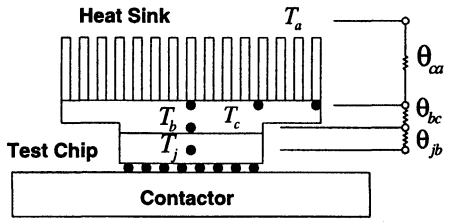

Fig. 1 Schematic of experimental setup. The thermal test chip is placed into an electrical contactor and the heat sink is placed on top of the test chip. Air is then impinged on the heat sink at $Re_D = 4.5 \times 10^4$.

Received March 18, 1998; revision received July 24, 1998; accepted for publication July 27, 1998. Copyright © 1998 by the American Institute of Aeronautics and Astronautics, Inc. All rights reserved.

*Santa Clara Processor Division, M/S RN3-61, 2200 Mission College Boulevard.